Materials Chemistry and Physics 183 (2016) 110–120

Contents lists available at ScienceDirect

Materials Chemistry and Physics

journal homepage: www.elsevier.com/locate/matchemphys

Study of structural and optical properties of $CaMoO_4$ nanoparticles synthesized by the microwave-assisted solvothermal method

G. Botelho [a, *], I.C. Nogueira [b], E. Moraes [a], E. Longo [c]

[a] INCTMN-UFSCar, Universidade Federal de São Carlos, P.O. Box 676, 13565-905, São Carlos, SP, Brazil
[b] Instituto Federal do Maranhão, PPG em Engenharia de Materiais, 65030-005, São Luís, MA, Brazil
[c] INCTMN-UNESP, Universidade Estadual Paulista, P.O. Box 355, CEP, 14801-907, Araraquara, SP, Brazil

HIGHLIGHTS

- Effect of propane-1,3-diol in the synthesis of nanoparticles by a rapid method.
- Utilization of first-principles quantum mechanical calculations.
- Investigation of photoluminescent properties of $CaMoO_4$ nanoparticles.

ARTICLE INFO

Article history:
Received 29 February 2016
Received in revised form
14 July 2016
Accepted 6 August 2016
Available online 6 August 2016

Keywords:
Nanostructures
Precipitation
Photoluminescence spectroscopy and optical properties

ABSTRACT

Calcium molybdate ($CaMoO_4$) nanoparticles were synthesized by using a rapid assisted-microwave solvothermal method. X-ray diffraction measurements, Fourier transform Raman and Fourier transform infrared spectroscopies, revealed that the samples all have a scheelite-type tetragonal structure. In addition, the data obtained from the Rietveld refinements revealed distortions of the [Ca–O] and [Mo–O] bonds that led, in turn, to distortions of the [CaO_8] and [MoO_4] clusters. The presence of irregular spherical-like $CaMoO_4$ nanoparticles and the corresponding crystallographic arrangement were confirmed and determined via transmission electron microscopy and high resolution transmission electron microscopy, respectively. First-principles quantum mechanical calculations based on the density functional theory at the B3LYP level were employed in order to understand the band structure and density of states of $CaMoO_4$ in the excited singlet and triplet states. Furthermore, the optical properties were investigated by performing ultraviolet–visible spectroscopy and photoluminescence (PL) measurements. Maximum PL emission of $CaMoO_4$ powders was detected in the green-region wavelength of the electromagnetic spectrum; this emission was attributed to the distorted [MoO_4] clusters.

1. Introduction

Calcium molybdate ($CaMoO_4$) crystallizes in a tetragonal structure, which is described by the $I4_1/a$ space group. This material has received significant attention from the scientific community, owing to its photoluminescence emissions in the visible region of the electromagnetic spectrum, at room temperature. As such, this material is well-suited for use as white light-emitting diodes (WLEDs) [1], light amplification by stimulated emission radiation (LASERs) [2], and hosts for lanthanide activated LASERs [3].

Several processes, such as the use of polymeric precursors [4], citrate complex using microwave irradiation [5], coprecipitation [6], sonochemical [7], hydrothermal/solvothermal [8], and microwave-hydrothermal/solvothermal methods [9–11], have been used to synthesize $CaMoO_4$ powders. Among them, the microwave assisted methods is considered an excellent strategy for the preparation of various ceramics oxides of controlled morphology. In the microwave-hydrothermal method, crystalline materials are obtained under high pressure and with microwave heating, using water as a solvent. When any other solvents are used, the process is referred to as microwave-solvothermal method [12,13] and, in this case, the solvent plays an integral role in the particle growth processes. Organic solvents have been used in the synthesis of $CaMoO_4$ powders, in order to obtain materials with small particles size and a narrow distribution of sizes [6,8,9,11,14–17]. For example, Thongtem et al. [17] obtained small

* Corresponding author.
E-mail address: gleice.lorena@gmail.com (G. Botelho).

http://dx.doi.org/10.1016/j.matchemphys.2016.08.008
0254-0584/

dispersed nano-particles by preparing $CaMoO_4$ powders via cyclic microwave radiation in propane-1,2-diol and NaOH. Furthermore, Phuruangrat et al. [9] reported that $CaMoO_4$ nanoparticles with average size of 28 nm, were obtained through synthesis in ethylene glycol under microwave radiation. Based on these previously published results, we propose a simple methodology to obtain $CaMoO_4$ using a low-temperature system, a short processing time and an organic solvent (propane-1,3-diol - PD) to control the particle morphology. Moreover, the PD solvent has favorable interactions with microwave radiation.

Therefore, in this paper, we present the synthesis of $CaMoO_4$ in PD solvent, by means of a microwave-assisted solvothermal (MAS) method at 120 °C for various times. These powders were characterized via X-ray diffraction (XRD), Fourier transform Raman (FT-Raman), and Fourier transform infrared (FT-IR) spectroscopies, transmission electron microscopy (TEM), ultraviolet–visible (UV–Vis) absorption spectroscopy, and PL measurements at room temperature. These results obtained were then correlated with those obtained by performing first-principles density functional theory calculations.

2. Materials and methods

2.1. Synthesis of $CaMoO_4$ powders

$CaMoO_4$ powders were prepared by applying the MAS method at 120 °C for various times, in the presence of propane-1,3-diol. Sodium molybdate dihydrate [$Na_2MoO_4 \cdot 2H_2O$] (99.5% purity, Aldrich) and calcium acetate monohydrated [$Ca(CH_3COO)_2 \cdot H_2O$] (99.0% purity, Mallinckrodt Chemicals) were used as the precursors. Initially, 2.5×10^{-3} mol of $Na_2MoO_4 \cdot 2H_2O$ and 2.5×10^{-3} mol of $Ca(CH_3COO)_2 \cdot H_2O$ were dissolved in 100 mL of propane-1,3-diol [$CH_2(CH_2OH)_2$] (99.9% purity, J. T. Baker). This solution was then stirred for 5 min at room temperature, in order to obtain a homogeneous mixture. The resulting solution was transferred to a Teflon autoclave, which was sealed and placed inside a microwave system (2.45 GHz, 800W) [18]. The systems were processed at 120 °C for 10, 30, and 60 min, respectively, at a heating rate of 25 °C/min. The heating time is included in the processing time. The autoclave pressure was kept constant during the process. After processing, the autoclave was allowed to cool naturally to room temperature. The byproducts were removed by washing the suspensions with distilled water and acetone. The resulting white precipitates were collected and dried at 60 °C in a conventional furnace for few hours.

2.2. Characterization of $CaMoO_4$ powders

The $CaMoO_4$ powders were characterized via X-ray diffraction (Rigaku-DMax/2500PC, Japan) performed over 2θ ranging from 10 to 75° and at a scan rate of 2.0°/min, using Cu Kα radiation (λ = 1.5406 Å). The Rietveld refinements were performed, using the general structure analysis (GSAS) program, on patterns obtained at scan rate of 0.2°/min for 2θ ranging from 10° to 110°. In addition, FT-Raman spectroscopy (Bruker-RFS 100, Germany) was conducted by using a Nd:YAG laser (λ = 1064 nm) that has a maximum output power of 100 mW. The spectra were measured at wavenumbers ranging from 50 cm^{-1} to 1.200 cm^{-1}. The FT-IR (Bruker-Equinox 55 spectrometer) and UV–vis (Varian spectrophotometer model Cary 5G, USA), spectroscopies were performed in transmittance mode at wavenumbers ranging from 200 cm^{-1} to 2000 cm^{-1}, and diffuse reflection mode, respectively. Furthermore, the morphologies of powders were examined by using a transmission electron microscope (model CM200, Philips, USA) operated at 200 kV. The crystallographic arrangement of $CaMoO_4$ nanoparticles was determined via high resolution transmission electron microscopy (HR-TEM). Moreover, the PL measurements were performed with a Monospec 27 monochromator (Thermal Jarrel Ash, USA) coupled to a R446 photomultiplier (Hamamatsu Photonics, Japan). A krypton ion laser (Coherent Innova 90 K, USA) (λ = 350 nm), with a maximum output power of 500 mW, was used as the excitation source. These measurements were all performed at room temperature.

2.3. Computational method

The periodic density functional theory (DFT) calculations were performed with the Becke's three parameter hybrid non-local exchange functional, combined with the Lee-Yang-Par gradient-corrected correlation function B3LYP [19,20]; this approach has proven to be very effective in addressing the present challenging problem. The electronic structures were calculated by using the CRYSTAL09 code [21]. In this work, the atomic centers were described by the following electronic basis sets: HAYWSC-31d1G HABAS (1998) for calcium, HAYWSC-311 (d31)G CORA (1997) for molybdenum, and 8–411 TOWLER (1994) for oxygen atoms, as obtained from the Crystal web site [22]; PS corresponds to the Hay & Wadt's non-relativistic small core pseudopotential [23]. During the calculations, the internal coordinates of the atoms as well as the lattice parameters (*a, b, c*) and angle were successively optimized (*CELLONLY* keyword crystal). Two systems with different excited states, i.e., singlet and triplet, were optimized by using the *SPINLOCK* keyword crystal.

The diagonalization of the Fock matrix was performed at adequate k-point grids in the reciprocal space, using a Pack-Monkhorst/Gilat shrinking factor of IS = ISP = 4. The threshold values controlling the accuracy of the calculation of Coulomb and exchange integrals were set to 10^{-6} (ITOL1 to ITOL4) and 10^{-12} (ITOL5); these values ensured a convergence in total energy better than 10^{-8} a. u. The percentage of Fock/Kohn–Sham matrix mixing was set to 40 (IPMIX = 40) [23]. Furthermore, triplet calculations were performed using SPIN and SPINLOCK = 2 keywords.

3. Results

3.1. X-ray diffraction and Rietveld refinement analyses

Fig. 1 shows the XRD patterns of $CaMoO_4$ powders obtained

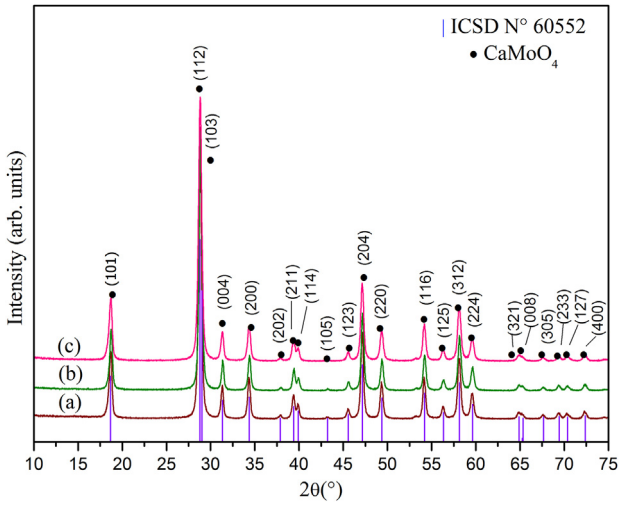

Fig. 1. XRD patterns of $CaMoO_4$ powders obtained by applying the MAS method for (a) 10 min, (b) 30 min, and (c) 60 min.

after various times. In agreement with the Inorganic Crystal Structure Database (ICSD) No. 60552 [24], the patterns were all indexed to the scheelite-type tetragonal structure whose symmetry is described by the space group $I4_1/a$. The patterns exhibit sharp peaks that are characteristic of materials with a high degree of crystallinity. Peaks corresponding to secondary phases were absent from the patterns.

The Rietveld refinement [25] method was used to explain possible differences in the MAS-processing-induced structural arrangements of $CaMoO_4$ powders. This refinement was performed by using the general structure analysis (GSAS) program with the EXPGUI graphical interface [26]. Optimized parameters such as the scale factor, background, shift lattice constants, profile half-width parameters (u, v, w), isotropic thermal parameters, lattice parameters, strain anisotropy factor, preferential orientation, and atomic functional positions, were used during the analyses. In addition, the background was corrected by using a Chebyschev polynomial of the first kind. The peak profile function was modeled by using a convolution of the Thompson-Cox-Hastings pseudo-Voigt (pV-TCH) [27] with an asymmetry function, described by Finger, which accounts for the asymmetry resulting from axial divergence [28].

The Rietveld refinements of $CaMoO_4$ powders obtained by applying the MAS method for various times are shown in Fig. 2 (a–c).

The measured diffraction patterns are well-matched to the ICSD No. 60552 [24]. However, significant deviation occurs in the low-angle regime, where the most intense peaks are located. This deviation is attributed to the characteristics of the patterns, which exhibit narrow peaks and high intensity. In general, the XRD pattern corresponding to the experimentally determined and the theoretically calculated data are almost identical, as indicated by the line Obs-Calc. The results of the refinements are summarized in Table 1 and further details are provided in the Supporting Information (Tables S1–S3).

The high quality of the refinements is revealed by the statistical fitting parameters (R_{wp}, R_p, R_{Bragg}, and χ^2) in Table 1. Furthermore, the close correspondence between the determined lattice parameters and the unit cell volumes reported in the literature, confirms that the $CaMoO_4$ powders are crystallized in a scheelite-type tetragonal structure; this structure has four molecular formula units per unit cell ($Z = 4$) and its symmetry is described by the space group $I4_1/a$ [24]. These powders may contain defects, as evidenced by small changes in the parameters, owing possibly to the synthesis method and experimental conditions (high temperature, solvents, microwave radiation, etc.). In addition, variations in the atomic positions of the oxygen atoms were observed (Table S3). These variations may lead to various distortions of the Ca–O, and/or Mo–O bonds, and consequently to different levels of distortion of the $[CaO_8]$ and/or $[MoO_4]$ clusters in the lattice (Tables S1 and S2).

The results shown in Table 1 were used to model a schematic of the tetragonal $CaMoO_4$ structure (Fig. 3), using the Diamond Crystal and Molecular Structure Visualization software [29]. In this structure, each molybdenum atom is coordinated to four oxygens atoms, forming tetrahedral $[MoO_4]$ clusters. In these isolated $[MoO_4]$ clusters, tetrahedrons have T_d - symmetry, except when located in

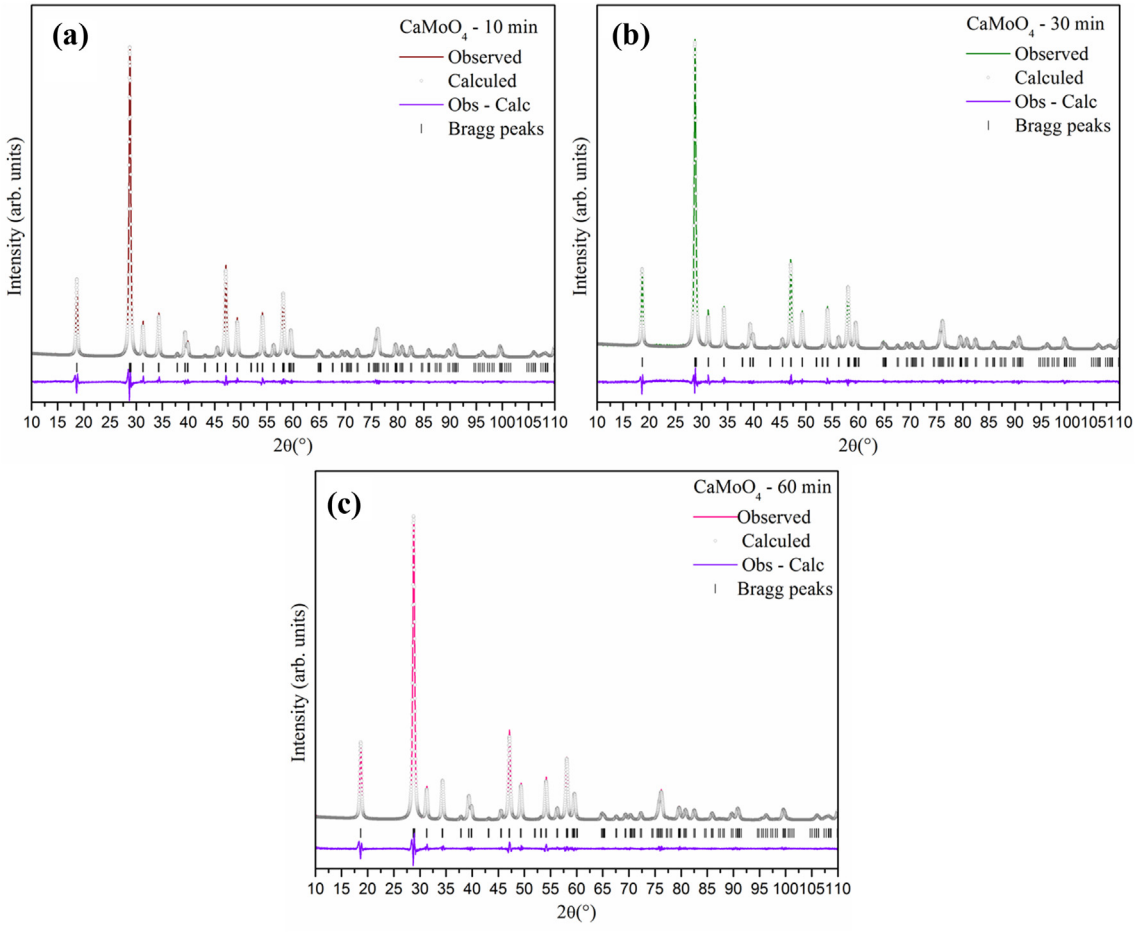

Fig. 2. Rietveld refinements of $CaMoO_4$ powders obtained by applying the MAS method for (a) 10 min, (b) 30 min, and (c) 60 min.

Table 1
Lattice parameters, unit-cell volume, and statistical parameters of quality obtained from the Rietveld refinement for $CaMoO_4$ powders obtained by applying the MAS method for various times.

Sample	Lattice Parameters		Cell volume (Å^3)	R_{Bragg} (%)	X^2	R_{wp} (%)	R_p (%)
	a, b (Å)	C (Å)					
$CaMoO_4$ -10 min	5.228 (3)	11.440 (9)	312.74 (1)	3.10	1.41	9.62	7.05
$CaMoO_4$ -30 min	5.228 (4)	11.440 (1)	312.73 (0)	6.57	1.58	12.15	8.65
$CaMoO_4$ - 60 min	5.228 (3)	11.440 (9)	312.73 (8)	2.86	1.34	9.28	6.78
$CaMoO_4$ - ICSD 60552	5.222 (1)	11.425 (3)	315.55	–	–	–	–

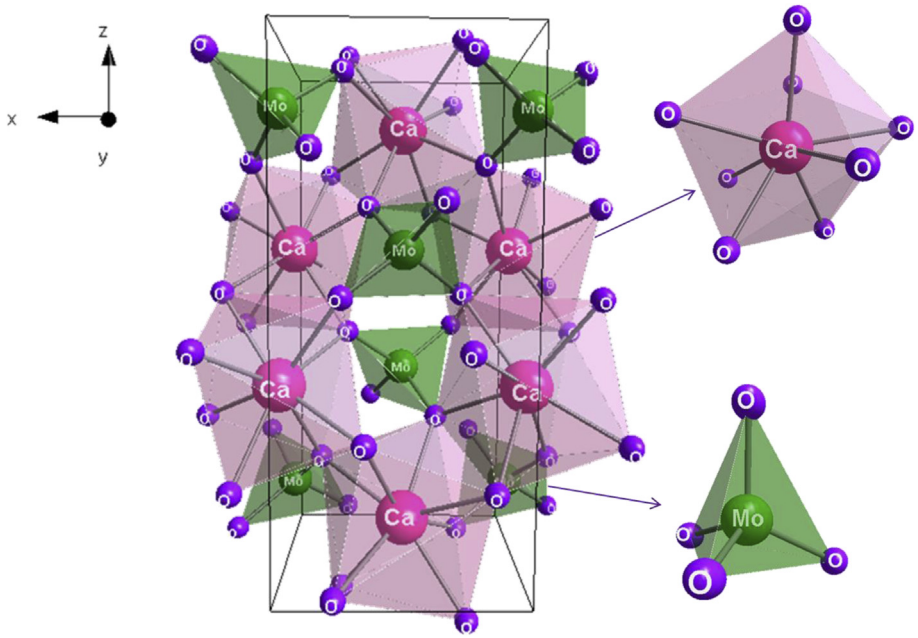

Fig. 3. Representation Schematic of the tetragonal $CaMoO_4$ structure, showing the [CaO_8] and [MoO_4] clusters.

scheelite structures where the point symmetry is reduced to S_4 [6,9,11,30,31]. On the other hand, each calcium atom is coordinated to eight oxygens atoms, thereby forming distorted deltahedral [CaO_8] clusters with 12 faces [14,31].

3.2. Fourier-transform Raman and infrared spectroscopies

According to group theory, the $CaMoO_4$ exhibits 26 vibrational modes [11,30,32] that are composed of non-degenerate A and B modes and doubly degenerate E modes. The A_g, B_g, and E_g vibrations are all Raman-active, whereas the $4E_u$ and $4A_u$ are infrared-active; the g and u subscripts indicate parity under inversion in centrosymmetric $CaMoO_4$ crystals. The $1E_u$ and $1A_u$ are acoustic modes, while the three Bu vibrations are forbidden infrared modes [30,32,33]. These vibrational modes are shown in the following equation.

$$C_{4h}^6\Gamma = 3A_g + 5A_u + 5B_g + 3B_u + 5E_g + 5E_u \quad (1)$$

Fig. 4 shows the FT-Raman spectra of $CaMoO_4$ powders obtained after various times. The Raman modes of the tetragonal $CaMoO_4$ structure can be classified into two groups, i.e., external and internal modes, based on the clusters present in the structure. The internal modes ($2A_g$, $3B_g$, and $2E_g$) correspond to the vibrations inside the [MoO_4] clusters, with the center of mass in the stationary state. The external modes ($1A_g$, $2B_g$, and $3E_g$) are attributed to vibrations of the [CaO_8] clusters [34].

Fig. 4 shows, the Raman-active modes are all observed, although some of the vibrational modes overlapped. The samples obtained after 30 and 60 min exhibited sharper bands (than those resulting from other times), which are indicative of a processing-induced increase in the short-range structural order. Moreover, the six low-frequency and seven high-frequency bands that occur at

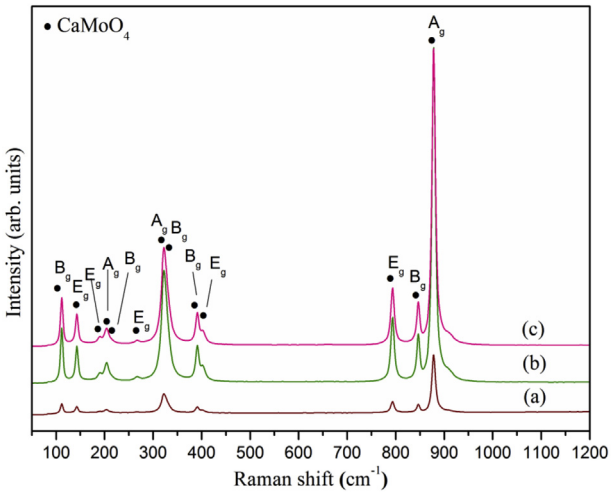

Fig. 4. FT-Raman spectra of $CaMoO_4$ powders obtained by applying the MAS method for (a) 10 min, (b) 30 min, and (c) 60 min.

wavenumbers of $\leq$270 cm^{-1} and $\geq$324 cm^{-1}, correspond to the external and internal modes, respectively. These results concur with those of previous studies [4,17,33,35].

Fig. 5 shows the FT-IR spectra of $CaMoO_4$ powders. Seven of the eight infrared-active vibrational modes possible for $CaMoO_4$, occur in the spectra of all the samples. The intense band that occurs at wavenumbers ranging from 790 cm^{-1} to 878 cm^{-1} represents an overlapping of two modes (E_u and A_u modes), and is attributed to antisymmetric stretching vibrations in the [MoO_4] clusters. The E_u and A_u modes that give rise to the sharp band observed at ~428 cm^{-1}, result from antisymmetric bending vibrations of the O–Mo–O bonds. Furthermore, the symmetric bending vibrations (A_u mode) and torsional vibrations (E_u mode) of the [MoO_4] clusters occur at wavenumbers of approximately ~330 cm^{-1} and 280 cm^{-1}, respectively. The band located at 240 cm^{-1} (E_u mode) is attributed to the translation of the [CaO_8] clusters. These results concur with those reported in previous studies [36]. The absorption bands that occur at wavenumbers ranging from 1200 cm^{-1} to 1700 cm^{-1}, result possibly from the presence of CO_2 that arises from the atmosphere and residual organic compounds (propane-1,3-diol); these bands are associated with the stretching modes of the C–O bond [11,30,32,34,37].

3.3. Transmission electron microscopy

Fig. 6 (a, c, and e) show low-magnification TEM micrographs of $CaMoO_4$ nanoparticles obtained after various times. The samples all exhibit irregular spherical-like nanoparticles. A growth mechanism was proposed for the $CaMoO_4$ nanoparticles based on TEM micrographs. Primary particles are formed from ions dissolved in the reaction mixture. The hydration energy is overcome by the strong electrostatics attraction between the precursor ions, to form primary particles. During the growth process, the freely rotating primary $CaMoO_4$ particles collide randomly and rearrange with respect to each other, forming discrete nanoparticles. When these nanoparticles coalesce to a common crystallographic orientation (oriented attachment - OA), the overall surface energy decreases. The growth process is referred to as imperfect OA, if different crystallographic orientations occur at the interface between the particles [38–40]. The high viscosity of the PD solvent (52 cP at 20 °C) may lead to decreased mobility and effective collision rates of the suspended primary particles. However, under the high temperatures employed by the MAS method, the viscosity of the PD solvent decreases, which in turn favors effective collision among, and growth of the nanoparticles [13]. This behavior is reinforced by junction (shown in the HR-TEM image in Fig. 6b)) in the interface contact among two nanoparticles. Fig. 6d and f indicate agglomeration between the nanoparticles.

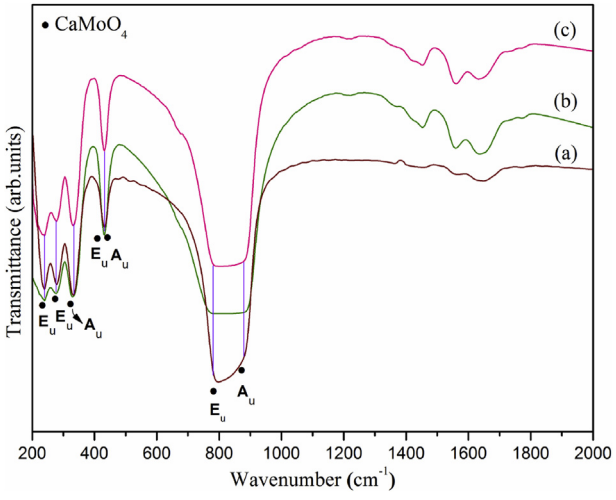

Fig. 5. FT-IR spectra of $CaMoO_4$ powders obtained by applying the MAS method for (a) 10 min, (b) 30 min, and (c) 60 min.

Marques et al. [11] reported that $CaMoO_4$ particles obtained via the coprecipitation method in H_2O and processed by means of a microwave-assisted hydrothermal technique at 140 °C for 1 h exhibited average sizes ranging from 1.25 μm to 4.75 μm. Longo et al. [10] obtained hierarchical assemblies of $CaMoO_4$ nano-octahedrons in H_2O using a microwave-assisted hydrothermal method in the presence of polyethylene glycol at 120 °C for various reaction times. These samples had average particle size distributions of 50–61 nm (width) and 68–127 nm (height). In our present work, it was possible to obtain nanometer scale particles with narrow size distributions by using PD solvent. Previous studies reported that the obtained morphology results from the interaction or adsorption of solvent molecules (with polymer characteristic) on some crystal faces, and the consequent preferential growth in specific directions. In our study, the organic solvent concentration is high, and all the crystal faces were capped by organic solvent. Therefore, the inhibition of particle growth along all crystallographic directions results in irregular spherical-like nanoparticles. Moreover, as mentioned previously, there is a decrease in the viscosity of PD solvent at high temperature. However, this viscosity is greater than that of H_2O in similar conditions. These changes lead, in turn, to a decrease in the particle sizes when compared to syntheses in an aqueous media [11,16,41–43].

In order to achieve a high efficiency in this microwave-assisted solvothermal system, it is necessary for the reaction mixture to have dipoles (polar solvent molecules) and/or charged particles (ions). During interactions between the molecular dipoles and the microwave radiation, the amount of heat generated is directly related to the ability of the dipoles to align in the direction of the applied electric field. This ability at a given frequency and temperature is known as the loss tangent (tan δ) [12,13]. Hence, the PD solvent (tan δ at 2.45 GHz and 25 °C = 1.30) [44] is a good candidate to be employed in microwave-assisted solvothermal systems. On the other hand, the dissolved charged particles oscillate under the influence of microwave radiation and collide with neighboring molecules or atoms to produce heat. Microwave heating also causes acceleration of reaction rates due to thermal effects, causing the formation of $CaMoO_4$ to occur more rapidly. Moreover, this synthesis is easily controlled through a number of different reaction parameters, allowing for a hight degree of reproducibility [12,13].

The average crystal size distribution was determined from the TEM micrographs by counting 100 nanoparticles that have excellent surface contour to ensure a good statistical sample size. As all samples contain irregular spherical-like nanoparticles, particle counting was performed along the length of each selected particle using ImageJ software. In all cases, particle size counting can be described by a log-normal distribution (Fig. 7(a–c)). The determined average particle sizes, 33.9 nm (10 min), 36.9 nm (30 min), and 35.8 nm (60 min), indicate that growth is more pronounced at long processing times than at short ones.

3.4. Ultraviolet–visible absorption spectroscopy

The band gap energy (E_{Gap}) values were experimentally calculated by using the Kubelka-Munk (K-M) function [45] and the Wood-Tauc method [46]. The diffuse reflectance measurements were converted to the K-M function by using the following equation:

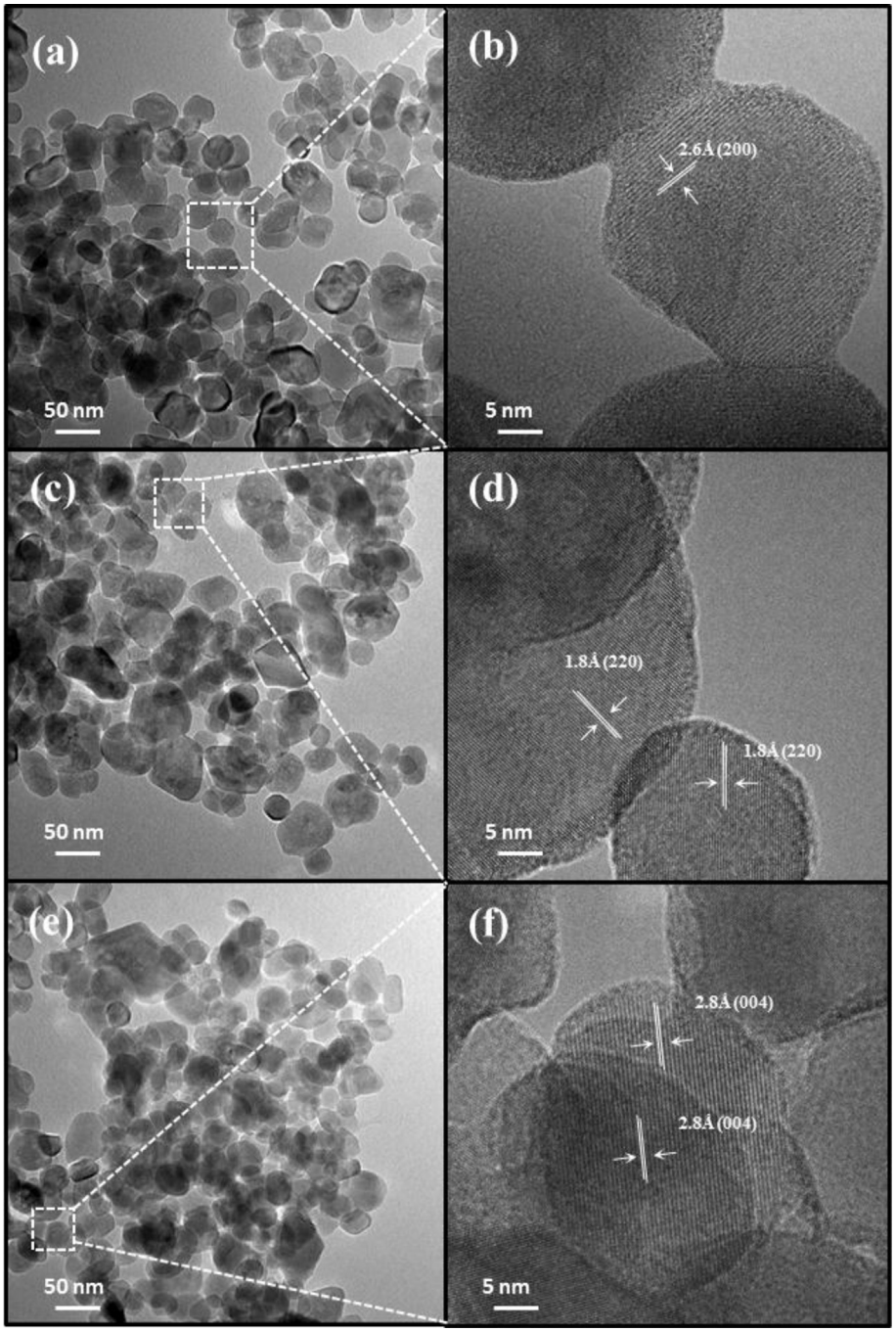

Fig. 6. Low-magnification TEM images of $CaMoO_4$ powders obtained by applying the MAS method for (a) 10 min, (c) 30 min, and (e) 60 min. HR-TEM images of $CaMoO_4$ powders obtained by applying the MAS method for (b) 10 min, (d) 30 min and (f) 60 min.

$$F(R_\infty) = \frac{(1-R_\infty)^2}{2R_\infty} = \frac{K}{S} \quad (2)$$

where $F(R_\infty)$ is the K-M function or absolute reflectance of the sample; R_∞ is the diffuse reflectance ($R_\infty = R_{sample}/R_{MgO}$), employing the magnesium (MgO) oxide as the standard sample; K is the molar absorption coefficient and S is the scattering coefficient. The Wood-Tauc method was subsequently employed, by using the following equation:

$$\alpha h\nu = C_1 (h\nu - E_{gap})^n \quad (3)$$

where α is the linear absorption coefficient; hν is the photon energy; C_1 is a proportionality constant and n is a constant associated with the different types of electronic transitions [n = 1/2 (direct allowed), n = 3/2 (direct forbidden), n = 2 (indirect allowed), and n = 3 (indirect forbidden)]. Previous experimental and theoretical studies reported that the molybdates exhibit a direct electronic transition, for which n = 1/2 [4,11,36]. Combining equations (2) and (3) gives:

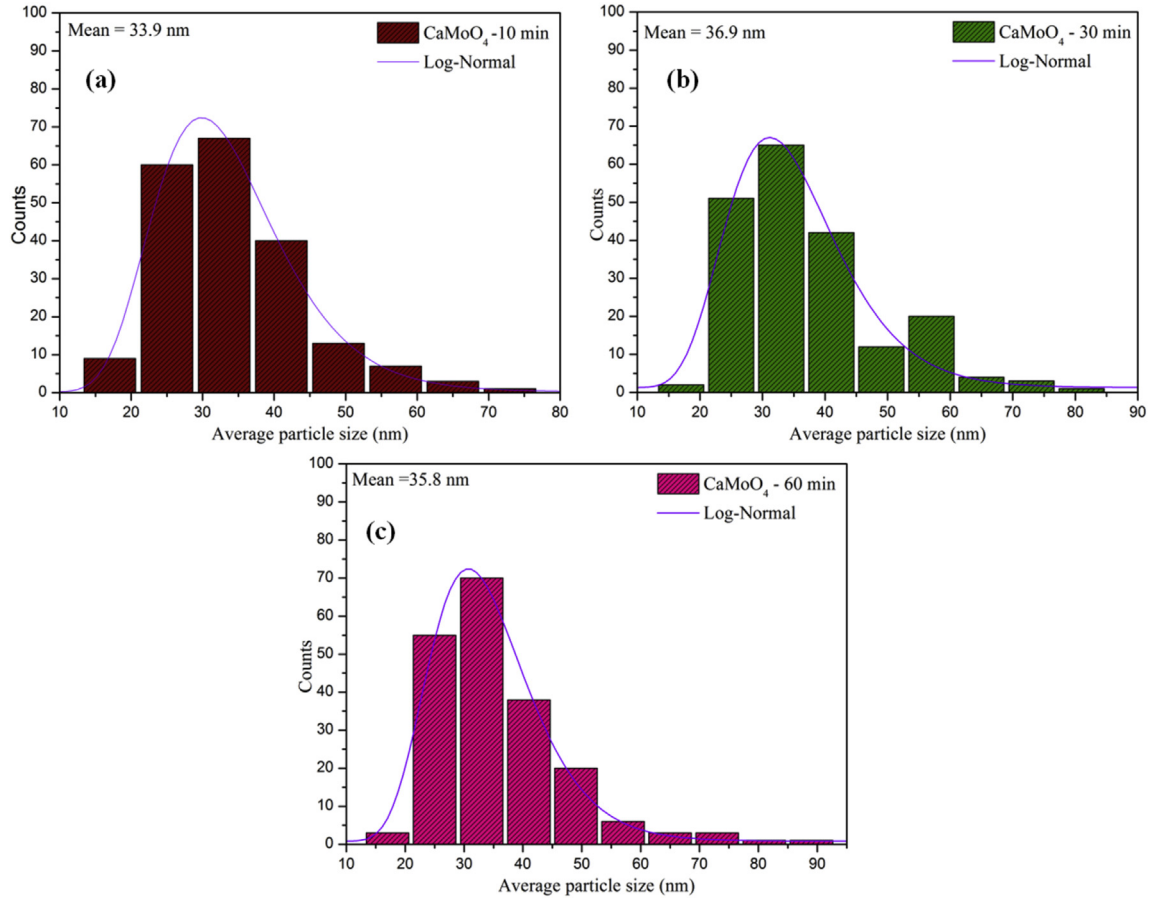

Fig. 7. Average size distribution of $CaMoO_4$ powders obtained by applying the MAS method for (a) 10 min, (b) 30 min, and (c) 60 min.

$$(F(R_\infty)h\nu)^2 = C_2(h\nu - E_{gap}) \quad (4)$$

where C_2 is a proportionality constant. Therefore, the experimental E_{gap} of $CaMoO_4$ powders can be determined by plotting $(F(R_\infty)h\nu)^2$ against hν, as shown in the Supporting Information (Fig. S1 (a–c)) and Table 2.

The band gap values are in good agreement with those published previously [4,11]. Marques et al. [11] studied the order-disorder structural transformation of $CaMoO_4$ crystals using theoretical models. These authors, attributed E_{gap} value to the redistribution of intermediary energy levels between the valence and conduction band (VB and CB, respectively); this redistribution results from the displacement of the Mo atoms along the x-, y-, and z-axes. The band gap values determined in the present study may therefore have a direct influence on the structural defects of $CaMoO_4$, as indicated by the results of the Rietveld refinement. However, the electronic levels can be thoroughly understood only by performing theoretical calculations.

Table 2
Band gap energy values of $CaMoO_4$ powders.

Sample	E_{gap} (eV)
$CaMoO_4$ – 10 min	3.93
$CaMoO_4$ – 30 min	3.92
$CaMoO_4$ – 60 min	3.90

3.5. Band structure and the density of states (DOS)

Fig. 8 shows the band structure and the DOS, projected on the $CaMoO_4$ atoms, for the singlet and triplet structures. The singlet state has a direct gap (Γ→Γ) of 4.90 eV. However, the triplet state has an indirect gap (Z→Γ) of 3.91 eV for alpha electrons and a direct gap (Γ→Γ) of 4.09 eV for the beta electrons. These data confirm that the reduction in the E_{gap} in the triplet state is associated with the appearance and redistribution of intermediary energy levels between the VB and the CB; this redistribution results from distortions in the material that leads to the formation of excited clusters. An analysis of the DOS projected on the atoms reveals that the maximum VB arises mainly from the O 2p orbitals. The singlet and triplet states of the CB arise from the Mo and O atoms.

3.6. Charge density maps and photoluminescence properties

Fig. 9 (a–c) shows the two-dimensional electron density maps obtained along the (010) plane in the $CaMoO_4$ singlet state, alpha electrons of the triplet state, and beta electrons of the triplet state models, respectively. The color scale of each map represents zones of high and low electronic densities, i.e., the blue and red regions have a high electronic density and no electronic charge, respectively. The cross-section of the three $[MoO_4]$ clusters considered in the models can be clearly identified from projections along the (010) plane. The covalent interaction of O with Mo atoms is visible in the elliptical light-blue regions. Moreover, the $[MoO_4]$ singlet and $[MoO_4]$ triplet clusters have similar electronic distributions,

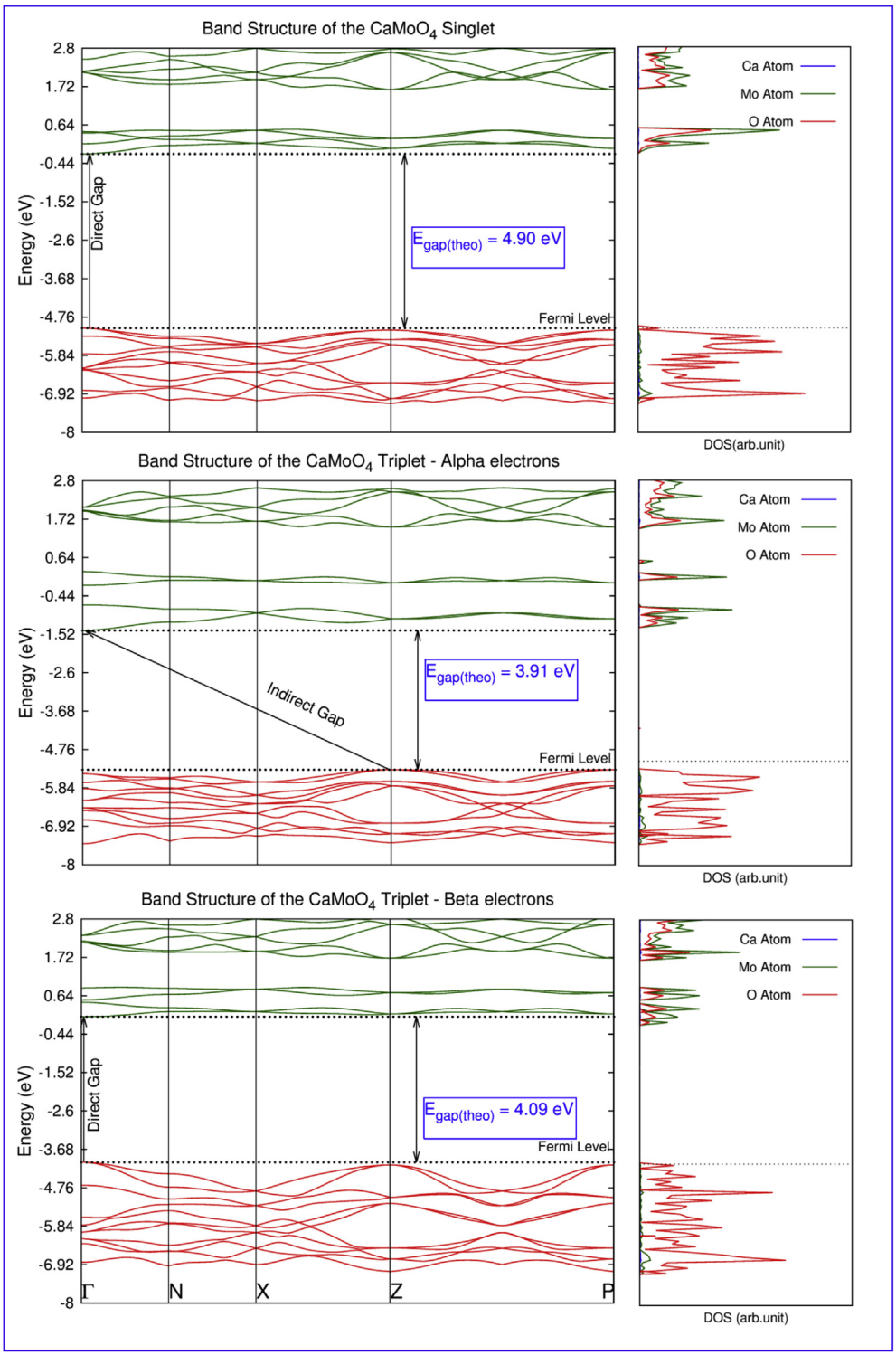

Fig. 8. Band structure and density of states of $CaMoO_4$ in the singlet and triplet states.

owing to the slight equivalency of the Mo–O bond distances (Fig. 9). In contrast, the perturbation in the system arising from the excited electron on the Mo atom resulted in the inhomogeneous electron distribution of the [MoO_4] clusters (referred to as $[MoO_4]_d^{\cdot}$). This inhomogeneity led in turn to the formation of $h^{\bullet}$ (Fig. 9b–c). Polarization is generated in the structure, via this defect, owing to the charge transfer from the perturbed ($[MoO_4]_d^{\cdot}$) to the unperturbed ($[MoO_4]_d^{\cdot}$) clusters (formation of $e' - h^{\bullet}$ pairs) [47].

Fig. 10 (a) shows the room-temperature PL spectra of $CaMoO_4$ powders. The samples all exhibit broad band emission, with maximum emissions occurring in the green-region wavelength of the electromagnetic spectrum (504–516 nm). Compared to the literature, our samples presented a blue shift that is potentially associated with differences synthesis in the synthetic method

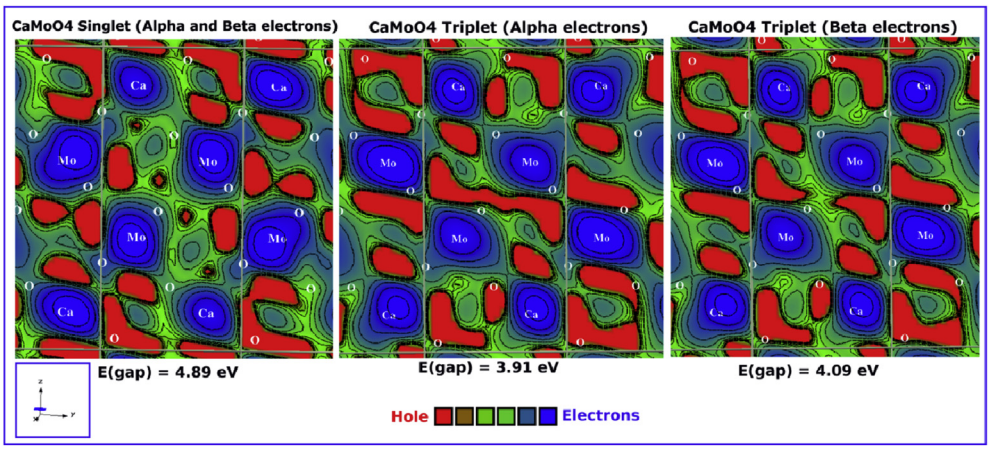

Fig. 9. Charge density maps of $CaMoO_4$ in the (a) singlet state, (b) alpha electron triplet state, and (c) beta electron triplet state.

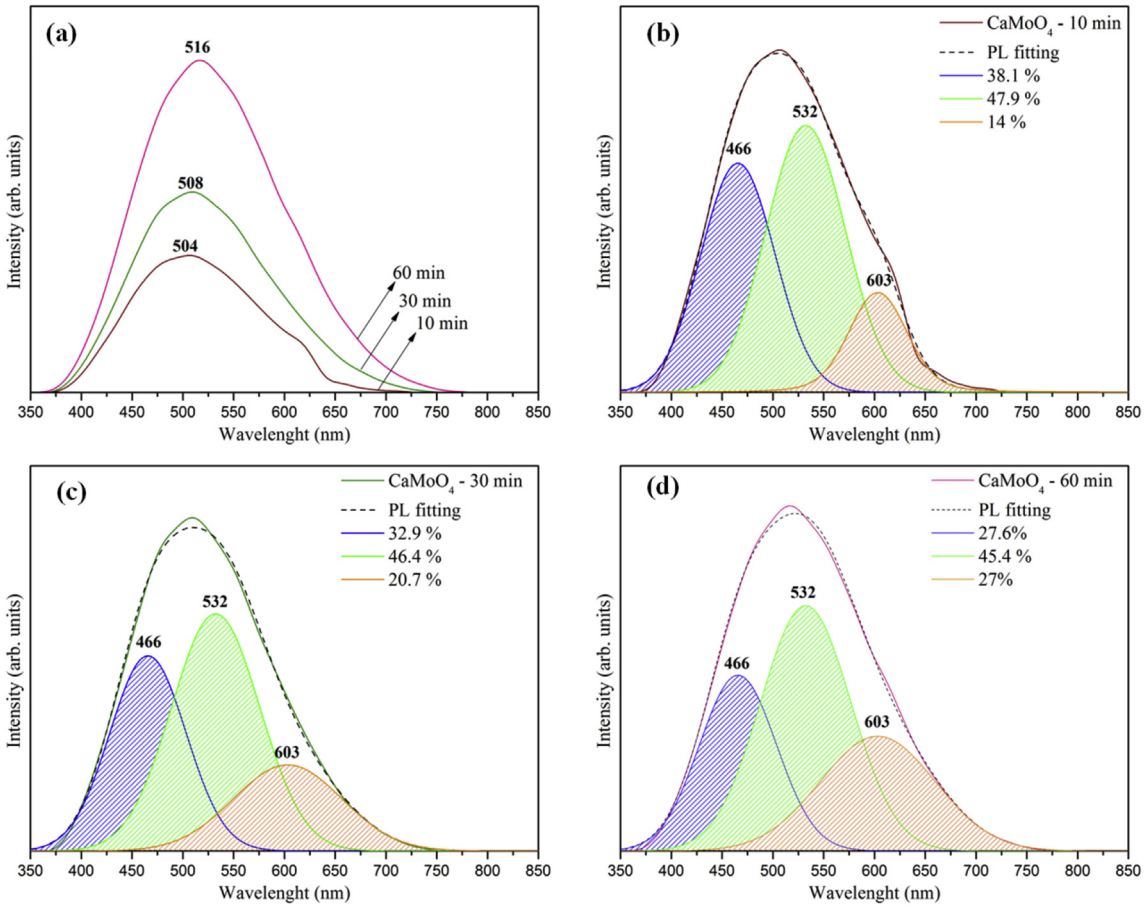

Fig. 10. (a) PL spectra of $CaMoO_4$ powders obtained by applying the MAS method for various times. Deconvolutions of the PL spectra of $CaMoO_4$ powders obtained after (b) 10 min, (c) 30 min, and (d) 60 min, showing the area percentage of each color component of the emission peak.

utilized and the morphologies obtained [10,13]. The PL properties of $CaMoO_4$ powders were thoroughly examined by using the PickFit software to deconvolute the PL curves. The area percentage of each color component corresponding to the emission peak (Fig. 10 (b–d)) was then determined from the deconvoluted curves. The results revealed contrasting trends for the blue and orange regions, i.e., the corresponding area percentages decreased from 38.1% to 27.6% and increased from 14% to 27%, respectively, with increasing synthesis time. However, the percentage of the green region changed only slightly from 47.9% to 45.4%. These trends indicate that the samples all have a high percentage of deep-level defects, whose density increases with increasing synthesis time; the occurrence of these defects varies with the percentage of green and orange components. Similarly, reductions in the density of shallow-level defects are associated with reductions in the percentage of the blue component.

Many previous experimental and theoretical studies have explained the origin of the PL properties of $CaMoO_4$ [4–6,9–11,15,42,48–50]. Some studies have attributed the PL emission to the charge-transfer transitions within the $[MoO_4^{2-}]$ complex (ions) [5,9,49,50]. The morphology also influences the PL properties [5,10,49,50]. However, other scientific studies have attributed the PL emission to a slight intrinsic distortion of the tetrahedral $[MoO_4]$ clusters [4,10,11,51]. These distortions stem from several factors, such as the: excellent interaction of the Mo atoms with microwave irradiation, continuous dissolution and recrystallization mechanism during the crystal growth processes, and the use of organic solvents. The corresponding defect-induced break in the symmetry may lead to the formation of intermediary energy levels within the forbidden band gap, as previously discussed in our theoretical calculations and reported in the literature [37,52]. Therefore, these distortions may play an important role in the formation of deep-level defects, and thereby influence the green PL emission process in the $CaMoO_4$ nanoparticles.

4. Conclusion

$CaMoO_4$ nanoparticles were successfully prepared by means of a microwave-assisted solvothermal method, applied for short times. The samples exhibited both long- and short-range structural order, as revealed by XRD measurements, as well as FT-Raman and FT-IR spectroscopies. In addition, the structural refinement data indicated that the $[CaO_8]$ and $[MoO_4]$ clusters were slightly distorted. With regards to the morphology, the $CaMoO_4$ powders consist of irregular spherical-like nanoparticles, indicating that the organic solvent used in the synthesis has an effect on the particle size. The E_{Gap} results indicated that intermediary energy levels formed within the band gap, owing possibly to the experimental conditions. These experimental findings are articulated with the ab initio calculations, which show that the formation of defects is linked to the occurrence of excited states. This observation is confirmed by the appearance of an indirect band gap in the triplet state and perturbations in the system arising from the excited electrons in the Mo atoms resulting in the inhomogeneous electron distribution of the $[MoO_4]$ clusters. Moreover, the photoluminescence of the crystal structure was attributed to the polarization of clusters at mainly short and medium distances.

Acknowledgments

The authors are grateful to the INCTMN (2008/57872-1), FAPESP (2013/07296-2), CNPq (147001/2013-7; 573636/2008-7), and PNPD (1268069) for financially supporting this research.

Appendix A. Supplementary data

Supplementary data related to this article can be found at http://dx.doi.org/10.1016/j.matchemphys.2016.08.008.

References

[1] X.X. Ju, X.M. Li, W.L. Li, W.J. Yang, C.Y. Tao, Luminescence properties of $ZnMoO_4$:Tb^{3+} green phosphor prepared via co-precipitation, Mater. Lett. 65 (2011) 2642–2644.
[2] L.H.C. Andrade, M.S. Li, Y. Guyot, A. Brenier, G. Boulon, Optical multi-sites of Nd^{3+}-doped $CaMoO_4$ induced by Nb^{5+} charge compensator, J. Phys-Condes. Matter 18 (2006) 7883–7892.
[3] A.A. Ansari, M. Alam, Optical and structural studies of CaMoO4: Sm, CaMoO4: Sm@ CaMoO4 and CaMoO4: Sm@ CaMoO4@ SiO2 core–shell nanoparticles, J. Lumines. 157 (2015) 257–263.
[4] V.M. Longo, A.T. de Figueiredo, A.B. Campos, J.W.M. Espinosa, A.C. Hernandes, C.A. Taft, J.R. Sambrano, J.A. Varela, E. Longo, Different origins of green-light photoluminescence emission in structurally ordered and disordered powders of calcium molybdate, J. Phys. Chem. A 112 (2008) 8920–8928.
[5] J.H. Ryu, J.W. Yoon, C.S. Lim, W.C. Oh, K.B. Shim, Microwave-assisted synthesis of $CaMoO_4$ nano-powders by a citrate complex method and its photoluminescence property, J. Alloy. Compd. 390 (2005) 245–249.
[6] T. Thongtem, S. Kungwankunakorn, B. Kuntalue, A. Phuruangrat, S. Thongtem, Luminescence and absorbance of highly crystalline $CaMoO_4$, $SrMoO_4$, $CaWO_4$ and $SrWO_4$ nanoparticles synthesized by co-precipitation method at room temperature, J. Alloy. Compd. 506 (2010) 475–481.
[7] J. Zhang, L. Li, W. Zi, N. Guo, L. Zou, S. Gan, G. Ji, Self-assembled $CaMoO_4$ and $CaMoO_4$: Eu^{3+} hierarchical superstructures: facile sonochemical route synthesis and tunable luminescent properties, J. Phys. Chem. Solids 75 (2014) 878–887.
[8] Y.S. Luo, X.J. Dai, W.D. Zhang, Y. Yang, C.Q. Sun, S.Y. Fu, Controllable synthesis and luminescent properties of novel erythrocyte-like $CaMoO_4$ hierarchical nanostructures via a simple surfactant-free hydrothermal route, Dalton Trans. 39 (2010) 2226–2231.
[9] A. Phuruangrat, T. Thongtem, S. Thongtem, Preparation, characterization and photoluminescence of nanocrystalline calcium molybdate, J. Alloy. Compd. 481 (2009) 568–572.
[10] V.M. Longo, L.S. Cavalcante, E.C. Paris, J.C. Sczancoski, P.S. Pizani, M.S. Li, J. Andres, E. Longo, J.A. Varela, Hierarchical assembly of $CaMoO_4$ nano-octahedrons and their photoluminescence properties, J. Phys. Chem. C 115 (2011) 5207–5219.
[11] V.S. Marques, L.S. Cavalcante, J.C. Sczancoski, A.F.P. Alcantara, M.O. Orlandi, E. Moraes, E. Longo, J.A. Varela, M.S. Li, M. Santos, Effect of different solvent ratios (Water/Ethylene glycol) on the growth process of $CaMoO_4$ crystals and their optical properties, Cryst. Growth Des. 10 (2010) 4752–4768.
[12] M. Baghbanzadeh, L. Carbone, P.D. Cozzoli, C.O. Kappe, Microwave-assisted synthesis of colloidal inorganic nanocrystals, Angew. Chem. Int. Ed. 50 (2011) 11312–11359.
[13] I. Bilecka, M. Niederberger, Microwave chemistry for inorganic nanomaterials synthesis, Nanoscale 2 (2010) 1358–1374.
[14] L.S. Cavalcante, V.M. Longo, J.C. Sczancoski, M.A.P. Almeida, A.A. Batista, J.A. Varela, M.O. Orlandi, E. Longo, M.S. Li, Electronic structure, growth mechanism and photoluminescence of $CaWO_4$ crystals, Crystengcomm 14 (2012) 853–868.
[15] C.S. Lim, Microwave-assisted synthesis and photoluminescence of $MMoO_4$ (M=Ca, Ba) particles via a metathetic reaction, J. Lumines. 132 (2012) 1774–1780.
[16] Y. Sun, J.F. Ma, X.H. Jiang, J.R. Fang, Z.W. Song, C. Gao, Z.S. Liu, Ethylene glycol-assisted electrochemical synthesis of $CaMoO_4$ crystallites with different morphology and their luminescent properties, Solid State Sci. 12 (2010) 1283–1286.
[17] T. Thongtem, A. Phuruangrat, S. Thongtem, Characterization of $MMoO_4$ (M=Ba, Sr and Ca) with different morphologies prepared using a cyclic microwave radiation, Mater. Lett. 62 (2008) 454–457.
[18] E. Longo Da Silva, J. Arana Varela, D.K. De Araujo Almeida, D. Paschoalini Volanti, Microwave Aided Device for Hydrothermal Synthesis of Nanostructured Oxides, Particularly Obtaining Particles of Metal Oxides, Comprises Container, in Which Hydrothermal Reaction Takes Place, and Lid for Container, Univ. Estadual Paulista, Brazil, 2010, p. 19.
[19] A.D. Becke, Density-functional thermochemistry. III. The role of exact exchange, J. Chem. Phys. 98 (1993) 5648–5652.
[20] C. Lee, W. Yang, R.G. Parr, Development of the Colle-Salvetti correlation-energy formula into a functional of the electron density, Phys. Rev. B 37 (1988) 785–789.
[21] R. Dovesi, V. Saunders, R. Roetti, R. Orlando, C. Zicovich-Wilson, F. Pascale, B. Civalleri, K. Doll, N. Harrison, I. Bush, CRYSTAL09 (CRYSTAL09 User's Manual), University of Torino, Torino, 2009.
[22] Crystal - Basis Sets Library. http://www.crystal.unito.it/basis-sets.php (acessed 13.03.15).
[23] W.R. Wadt, P.J. Hay, Ab initio effective core potentials for molecular calculations. Potentials for main group elements Na to Bi, J. Chem. Phys. 82 (1985) 284–298.
[24] R.M. Hazen, L.W. Finger, J.W.E. Mariathasan, Hight-pressure crystal-chemistry of Scheelite-type tungstates and molybdates, J. Phys. Chem. Solids 46 (1985) 253–263.
[25] H.M. Rietveld, A profile refinement method for nuclear and magnetic structures,, J. Appl. Crystallogr. 2 (1969) 65–75.
[26] B.H. Toby, EXPGUI, a graphical user interface for GSAS, J. Appl. Crystallogr. 34 (2001) 210–213.
[27] P. Thompson, D.E. Cox, J.B. Hastings, Rietveld refinement of debye-scherrer synchrotron X-ray data from AL_2O_3, J. Appl. Crystallogr. 20 (1987) 79–83.
[28] L.W. Finger, D.E. Cox, A.P. Jephcoat, A Correction for powder diffraction peak asymmetry due to axial divergence, J. Appl. Crystallogr. 27 (1994) 892–900.
[29] K. Brandenburg, H. Putz, Diamond. Version 3.2g, University of Bonn, Germany, 2011.
[30] T.T. Basiev, A.A. Sobol, Y.K. Voronko, P.G. Zverev, Spontaneous Raman spectroscopy of tungstate and molybdate crystals for Raman lasers, Opt. Mater. 15 (2000) 205–216.
[31] M. Bomio, R. Tranquilin, F. Motta, C. Paskocimas, R. Nascimento, L. Gracia, J. Andres, E. Longo, Toward understanding the photocatalytic activity of $PbMoO_4$ powders with predominant (111),(100),(011)(110) facets. A combined experimental and theoretical study, J. Phys. Chem. C 117 (2013) 21382–21395.
[32] V. Panchal, N. Garg, S.M. Sharma, Raman and X-ray diffraction investigations

on $BaMoO_4$ under high pressures, J. Phys-Condes. Matter 18 (2006) 3917–3929.
[33] E. Sarantopoulou, C. Raptis, S. Ves, D. Christofilos, G.A. Kourouklis, Temperature and pressure dependence of Raman-active phonons of $CaMoO_4$: an anharmonicity study, J. Phys-Condes. Matter 14 (2002) 8925–8938.
[34] P. Tarte, M. Liegeois, Vibrational Studies of molybdates, tungstates and related compounds - 1: new infrared data and assignments for scheelite-type compounds $X^{II}MoO_4$ and $X^{II}WO_4$, Spectrochim. Acta A 28 (1972) 2029–2036.
[35] P.G. Zverev, Vibronic relaxation of Raman modes in $CaMoO_4$ and $PbMoO_4$ molecular ionic crystals, Phys. Status Solidi C 1 (2004) 3101–3105.
[36] A.P.A. Marques, F.V. Motta, E.R. Leite, P.S. Pizani, J.A. Varela, E. Longo, D.M.A. de Melo, Evolution of photoluminescence as a function of the structural order or disorder in $CaMoO_4$ nanopowders, J. Appl. Phys. 104 (2008) 043505.
[37] M.R.D. Bomio, L.S. Cavalcante, M.A.P. Almeida, R.L. Tranquilin, N.C. Batista, P.S. Pizani, M.S. Li, J. Andres, E. Longo, Structural refinement, growth mechanism, infrared/Raman spectroscopies and photoluminescence properties of $PbMoO_4$ crystals, Polyhedron 50 (2013) 532–545.
[38] R.L. Penn, J.F. Banfield, Imperfect oriented attachment: dislocation generation in defect-free nanocrystals, Science 281 (1998) 969–971.
[39] C.J. Dalmaschio, C. Ribeiro, E.R. Leite, Impact of the colloidal state on the oriented attachment growth mechanism, Nanoscale 2 (2010) 2336–2345.
[40] R.L. Penn, J.A. Soltis, Characterizing crystal growth by oriented aggregation, CrystEngComm 16 (2014) 1409–1418.
[41] Y. Tian, B. Chen, H. Yu, R. Hua, X. Li, J. Sun, L. Cheng, H. Zhong, J. Zhang, Y. Zheng, T. Yu, L. Huang, Controllable synthesis and luminescent properties of three-dimensional nanostructured $CaWO_4:Tb^{3+}$ microspheres, J. Colloid Interf. Sci. 360 (2011) 586–592.
[42] J.G. Yu, X.F. Zhao, S.W. Liu, M. Li, S. Mann, D.H.L. Ng, Poly(methacrylic acid)-mediated morphosynthesis of $PbWO_4$ micro-crystals, Appl. Phys. A-Mater. 87 (2007) 113–120.
[43] L.S. Cavalcante, J.C. Sczancoski, M. Siu Li, E. Longo, J.A. Varela, beta-ZnMoO4 microcrystals synthesized by the surfactant-assisted hydrothermal method: growth process and photoluminescence properties, Colloid. Surf. A 396 (2012) 346–351.
[44] E. Grant, B.J. Halstead, Dielectric parameters relevant to microwave dielectric heating, Chem. Soc. Rev. 27 (1998) 213–224.
[45] L. Tolvaj, K. Mitsui, D. Varga, Validity limits of Kubelka–Munk theory for DRIFT spectra of photodegraded solid wood, Wood Sci. Technol. 45 (2011) 135–146.
[46] D. Wood, J. Tauc, Weak absorption tails in amorphous semiconductors, Phys. Rev. B 5 (1972) 3144–3151.
[47] A. Gouveia, J. Sczancoski, M. Ferrer, A. Lima, M. Santos, M.S. Li, R. Santos, E. Longo, L. Cavalcante, Experimental and theoretical investigations of electronic structure and photoluminescence properties of β-Ag2MoO4 microcrystals, Inorg. Chem. 53 (2014) 5589–5599.
[48] V.B. Mikhailik, H. Kraus, D. Wahl, M.S. Mykhaylyk, Studies of electronic excitations in $MgMoO_4$, $CaMoO_4$ and $CdMoO_4$ crystals using VUV synchrotron radiation, Phys. Status. Solidi. B 242 (2005) R17–R19.
[49] Y. Xiang, J. Song, G. Hu, Y. Liu, Synthesis of $CaMoO_4$ hierarchical structures via a simple slow-release co-precipitation method, Appl. Surf. Sci. 349 (2015) 374–379.
[50] X. Liu, L. Li, H.M. Noh, S.H. Park, J.H. Jeong, H.K. Yang, K. Jang, D.S. Shin, Synthesis and photoluminescence of novel 3D flower-like $CaMoO_4$ architectures hierarchically self-assembled with tetragonal bipyramid nanocrystals, Opt. Mater. 43 (2015) 10–17.
[51] A. Campos, A. Simoes, E. Longo, J.A. Varela, V. Longo, A. De Figueiredo, F. De Vicente, A. Hernandes, Mechanisms behind blue, green, and red photoluminescence emissions in $CaWO_4$ and $CaMoO_4$ powders, Appl. Phys. Lett. 91 (2007) 051923.
[52] J.C. Sczancoski, M.D.R. Bomio, L.S. Cavalcante, M.R. Joya, P.S. Pizani, J.A. Varela, E. Longo, M.S. Li, J.A. Andres, Morphology and blue photoluminescence emission of PbMoO4 processed in conventional hydrothermal, J. Phys. Chem. C 113 (2009) 5812–5822.